On the Rate Distribution Analysis of Kinetic Data Using the Maximum Entropy Method: Applications to Myoglobin Relaxation on the Nanosecond and Femtosecond Timescales

Anand T. N. Kumar, Leyun Zhu, J. F. Christian, Andrey A. Demidov, and Paul M. Champion*

Department of Physics, Northeastern University, Boston, Massachusetts 02115

Received: December 31, 2000; In Final Form: April 27, 2001

We discuss the application of the maximum entropy method (MEM) to the extraction of rate distributions from kinetics experiments on the nanosecond to femtosecond time scale. We first present simulations to show the effects of data truncation (typical of nanosecond experiments) on rate distributions recovered by MEM. The stretched exponential decay is considered as an example to demonstrate that if the true distribution of rates for the underlying process includes faster time scales than are contained within the experimental data set, MEM can introduce unwarranted features that extend into the slower regions of rate space. This observation has relevance to the application of MEM to obtain rate distributions from kinetic experiments involving the relaxation of complex molecules like proteins, where features in the distribution are sometimes interpreted as static distributions of protein conformational substates. As an experimental example, we present an MEM analysis of the temperature dependence of the geminate rebinding kinetics of carbonmonoxy myoglobin near room temperature and find a barrier height of 18 kJ/mol. We also consider the application of MEM to ultrafast pump−probe transient absorption data, where one needs to take into account the possibility of nonmonotonicity in the kinetics and the finite pulse autocorrelation width that effectively convolves into the observed material responses. The MEM analyses of the femtosecond photophysics of Mb and MbNO, monitored at several wavelengths in the visible region, are presented as examples.

I. Introduction

In the analysis of kinetic experiments involving the relaxation of complex materials like proteins and glasses, fits to the data using a few discrete exponentials are known to be inadequate, and one often has to resort to specific nonexponential models (such as the "stretched exponential") that fit the data directly in time domain. Another approach has been to seek a representation for the process in a space of decay rates, thus obviating the necessity of forcing a particular functional form to fit the data. In this case one, writes

$$I(t) = \int_0^\infty g(\lambda) \mathrm{e}^{-\lambda t}\, \mathrm{d}\lambda \qquad (1)$$

where $g(\lambda)$ is the distribution of rate constants for the process $I(t)$. Given an experimental $I(t)$, we would like to obtain the appropriate distribution $g(\lambda)$ that obeys eq 1. This essentially involves performing a numerical inverse Laplace transform on a noisy data function $I(t)$, which is known from information theory to be an ill-conditioned problem.[1] A large number of distributions can fit the data equally well, which implies a huge subspace of solutions, and regularization techniques[2] are required to obtain a smooth solution that is free of the noise induced artifacts. The maximum entropy method (MEM) is one such technique, where the smoothing function is the Shannon-Jaynes entropy.[3] MEM has been successfully applied in many situations where the inverse problem is highly degenerate, owing to the presence of noise in the data or the large parameter space one is working with. The application of Laplace inversion has been carried out in fields such as pulse-fluorimetry,[4] NMR spectroscopy,[5] and flash-photolysis studies of heme protein kinetics.[6−9] In particular, flash-photolysis studies monitor the transient absorption of a relaxing material (monitored at specific wavelengths) over time scales that are limited experimentally by laser pulse widths and detector response times. The MEM is used to obtain smooth rate distributions for the observed kinetics. Individual features (such as peaks) in the distribution are usually ascribed to static distributions of conformational substates. In low-temperature studies with heme proteins, these features are often interpreted as enthalpy barrier distributions for the quenched conformational substates of the protein.[6,9,10] As such, these features are an important factor in the interpretation of the kinetic data.

The advantage in the use of the Shannon-Jaynes entropy over other regularization functions is that it guarantees that the MEM solution does not contain structure beyond that demanded by the experimental information.[11] In the present work, we present MEM simulations (in the context of Laplace inversion) to point out problems that can occur when the short time experimental data is limited. The MEM reconstruction of kinetics that are governed by a broad distribution of rate constants, but suffer from insufficient data at shorter times (e.g., due to experimental limitations), can have artifactual features that do not represent the real distribution of rates in the system. This has relevance to the MEM analysis of flash photolysis and similar kinetic experiments, where the interpretation in terms of barrier heights is central. The purpose here is not so much to make a detailed study of the numerical nature of the artifacts, but to stress their

* Corresponding author. E-mail: champ@neu.edu.

10.1021/jp0101209 CCC: $20.00
Published on Web 07/19/2001

importance in applications related to Laplace inversion and suggest possible ways to check for their occurrence.

As an example, we focus on the "stretched exponential" type of relaxation, which has often been used to describe time-dependent (or series) relaxation in many complex systems.[12−15] Although a successful kinetic analysis, based on the rate representation given in eq 1, presumes the existence of an inhomogeneous distribution of rate constants in the system (parallel relaxation), this does not rule out the possibility that the relaxing system is homogeneous with time-dependent rates. The distinction between a homogeneous and heterogeneous ensemble can only be made through additional experiments (e.g., kinetic selection using multiple pulse protocols[14,16−18]). Nevertheless, a general representation such as eq 1 is still useful in testing for nonexponential behavior. Here, the motivation behind the choice of a stretched exponential is with the view to applying the present analysis to previous temperature-dependent studies of MbCO relaxation dynamics, where the nonexponential geminate recombination of CO to Mb at high temperatures was modeled using a stretched exponential.[14,15,17,19] However, the potential problems associated with MEM analysis exist quite generally for processes that have broad rate distributions with insufficient experimental data on short time scales. Thus, in addition to the stretched exponential, we also illustrate the effects of insufficient short time data by analyzing a kinetic process having a Gaussian distribution of decay amplitudes.

Finally, we present a MEM analysis of ultrafast pump−probe experiments on Mb and MbNO. We use an extended MEM algorithm that is capable of extracting positive and negative amplitude rate distributions (corresponding to bleaching and anti-bleaching signals) and allowing for convolution of the laser pulse autocorrelation function. The results of the MEM analysis on deoxyMb and MbNO data are presented as examples, and the possibility of nonexponential behavior in the photophysical and ligand rebinding processes is addressed.

II. Methods

A. Background. We give only a brief account of MEM here and refer the reader to the large literature related to the method for a more detailed discussion.[11,20,21] Since typical experimental data in kinetic studies stretch over several decades in time, it is appropriate to use a logarithmic rate space. Transforming the Laplace integral eq 1 to logarithmic space and writing the integral in the form of a discrete sum, we have

$$I(t) = \sum_{j=1}^{M} f_j e^{-\lambda_j t} \Delta(\log \lambda_j) \tag{2}$$

Here, M is typically on the order of the number of data points N. The spacings $\Delta(\log \lambda_j)$ are usually chosen to be a constant. The f_j's then constitute a distribution of rates in logarithmic rate space. The MEM proceeds as usual by defining the entropy

$$S = -\sum_{j=1}^{M} f_j \left[\ln\left(\frac{f_j}{F_j}\right) - 1 \right] \tag{3}$$

The F_j's are the so-called prior distribution, which are used to incorporate any previous knowledge that we may have about the rate distribution. In the absence of experimental data, maximizing the entropy function gives the solution $f_j = F_j$. The normalized mean square error between the model and the data is expressed as

$$\chi^2 = \frac{1}{N} \sum_{k=1}^{N} \frac{[I_f(t_k) - I_e(t_k)]^2}{\sigma_k^2} \tag{4}$$

where the subscripts e and f denote the experimental and the fit values of the function $I(t)$ and σ_k is the noise variance associated with the kth data point. With these two expressions, the MEM seeks to maximize the "functional" Q defined as

$$Q = S - \eta\chi^2 \tag{5}$$

where η is the Lagrange undetermined multiplier that is chosen to satisfy the constraint that $\chi^2 = 1$. With the number of parameters M of the same order as the number of available data N, the noise in the data results in a highly degenerate solution set[22] for a given χ^2. The addition of the entropy function helps extract a unique solution that is free of unwanted correlations. MEM is thus said to be maximally noncommittal with respect to unavailable information.

B. Implementation. The implementation of the MEM algorithm in the present study was carried out using a home-built program written in MATLAB (version 4.2). All calculations were carried out using double precision arithmetic. Rate distributions were obtained in logarithmic space. The algorithm was based on a straightforward Newton−Raphson optimization scheme to minimize $-Q = \eta\chi^2 - S$, where the Lagrange multiplier η is adjusted to satisfy the constraint that χ^2 be near unity (which is the optimal value for data with white Gaussian noise). The size of the discretized rate space was only of the order of 10^2, and hence, it was feasible to use the full Hessian matrix[22] $\nabla\nabla Q$ in calculating the steps. Line searches[22] were used to adjust the size of the steps. To begin with, η was set to be a small number of the order of σ^2 (where σ is the estimated noise variance in the data), and Q was optimized for this value. The value of η was then stepped iteratively and Q successively optimized until χ^2 reached a value close to 1. The initial guess for the unknown amplitudes f_j was chosen to be flat (typical value of 10^{-4}), and the prior distribution F_j was set equal to the initial guess. This choice of the prior distribution reflects our complete lack of previous knowledge about the rate amplitudes. The program was tested with various known distributions and was seen to provide accurate reconstructions for the rate amplitudes. An important aspect of MEM as revealed by simulations (see Figure 1a) is that even pure exponential decay processes have rate distributions with finite width (unless the data is completely noiseless). Broad rate distributions obtained by MEM therefore do not necessarily imply nonexponential dynamics. A useful test to verify this is to fit the data with exponential decays with the centroids of the distributions as the rates and the areas as weights. If the normalized χ^2 of the resulting fit is of the same order as that of the MEM fit, it can be concluded that the dynamics can be well described by simple exponentials. A more rigorous approach would be to obtain an estimate for the resolution (width) in the MEM rate space, in terms of the noise in the data. In this case, the dynamics are potentially exponential unless the variance of the MEM distribution is broader than the estimated resolution in rate space.

The mathematical form of the entropy function given in eq 3 forces the rate amplitudes to be positive, which restricts the application of MEM to monotonic decays. To extend the applicability of MEM to bipolar signals[23,24] that involve both

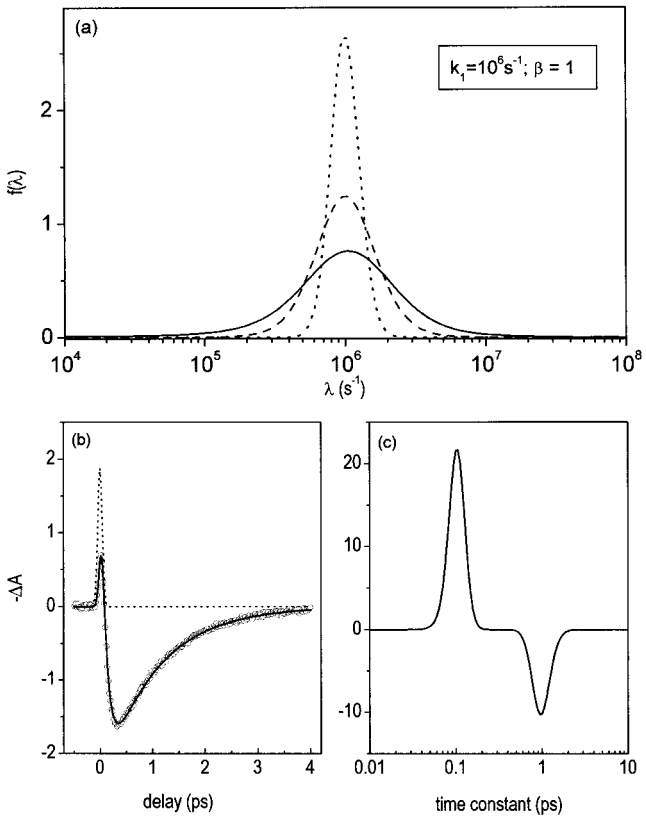

Figure 1. (a) MEM reconstruction for a simulated exponential decay with a rate of10^6 s^{-1}, with additive white Gaussian noise of $\sigma = 10^{-3}$(dotted line), 5×10^{-3} (dashed line) and 5×10^{-2} (solid line). (b) Simulated biexponential decay (circles) convolved with a 100 fs fwhm pulse autocorrelation (dotted line) is shown along with the MEM fit (solid line) using the bipolar algorithm. The decay constants are 0.1 and 1 ps, with an amplitude ratio of −0.5. (c) bipolar MEM distribution for the data shown in panel b.

positive and negative decays (such as seen in ultrafast transient absorption measurements), we write the rate amplitude f_j as the difference of two positive rate amplitudes f_j^{p} and f_j^{n}

$$f_j = f_j^{\mathrm{p}} - f_j^{\mathrm{n}} \tag{6}$$

This distribution is used in the fitting function (eq 2) that is subject to the χ-square test, and the entropy function is written as the sum of two separate entropies defined (as in eq 3) with respect to f^{p} and f^{n}. The optimization of Q defined in eq 5 is now carried out with the gradients and Hessian matrices defined in a $2 \times M$ dimensional space formed by the vectors $f' = (f^{\mathrm{p}}, f^{\mathrm{n}})$. The iterative steps in f' then determine the corresponding steps for the positive and negative distributions.

In addition to the bipolar signals, the applicability of MEM to kinetic data requires one to consider the finite laser pulse widths that effectively convolve into the response of the system. For ultrafast pump−probe data, we convolve the experimentally known pulse autocorrelation into the model fitting function eq 2, which then takes the form

$$I(t) = \sum_{j=1}^{M} f_j G(\lambda_j, t) \Delta(\log \lambda_j) \tag{7}$$

where $G(\lambda_j,t)$ is obtained by convolving the exponential (the response for delta function pulses) with the pulse autocorrelation $P(t)$

$$G(\lambda_j, t) = \int_0^\infty P(t - t') \exp(-\lambda_j t')\, \mathrm{d}t' \tag{8}$$

The Newton−Raphson optimization proceeds as before, with minor modifications to the gradients and the Hessian used in the search algorithm.[25]

In Figure 1b,c, we present a simulation to demonstrate the efficiency of this algorithm in recovering bipolar rate constants from a convolved data set. A bimodal rate process with rate constants 0.1 and 1 ps and amplitude ratio $A_2/A_1 = -1/2$, convolved with a 100 fs fwhm Gaussian pulse, was used to generate the simulated data shown in Figure 1b. The rate constants and the noise level were chosen to represent a typical pump−probe study. It is seen from Figure 1c that the MEM accurately reproduces the rate constants, the faster of which is equal to the pulse width itself.

III. Results and Discussion

A. Simulations with a Gaussian Rate Distribution. For the first nonexponential simulation in the present study, data of the stretched exponential form

$$I(t) = \mathrm{e}^{-(k_1 t)^{\beta}} \tag{9}$$

were generated, with $k_1 = 10^6$ s^{-1} and $\beta = 1/2$ (the choice being based on typical values previously obtained for CO geminate recombination to Mb[14]), and white Gaussian noise with $\sigma = 10^{-3}$ was added. The MEM solution was then obtained for sets of renormalized data with successively increasing truncations[26] of the short time data points.

To test the accuracy of the MEM rate distribution, we calculate the analytic Laplace inverse of the stretched exponential. The inverse Laplace transform is expressed as the integral

$$g(\lambda) = \frac{-i}{2\pi} \int_{\mathrm{Br}} e^{\lambda t} I(t)\, \mathrm{d}t \tag{10}$$

where the integration is carried out over the appropriate Bromwich contour.[27] The Laplace inverse of the stretched exponential for general $0 < \beta < 1$ has not been obtained in a closed form, and only series approximations exist.[28] However, for the case $\beta = 1/2$, the analytic inverse is obtained using eq 10, and the result is

$$g(\lambda) = \frac{1}{2}\left(\frac{k_1}{\pi}\right)^{1/2} \frac{\exp(-k_1/4\lambda)}{\lambda^{3/2}} \tag{11}$$

which is an asymmetric bell shaped curve with a maximum at $\lambda = k_1/6$. Before we compare this expression with the MEM rate distribution, we must keep in mind that the MEM obtains a solution $f(\lambda)$ in log rate space, whereas the Laplace inverse $g(\lambda)$ is in linear rate space. The relationship between the two distributions follows immediately from the change of variables in going from log to linear space and is given by

$$g(\lambda) = \frac{f(\lambda)}{(\lambda \ln 10)} \tag{12}$$

It is worth noting from this relation that the linear space distribution $g(\lambda)$ is narrower than the log space distribution. Figure 2a shows the analytic expression in linear (full line) and log space (dashed line) for a stretched exponential with $\beta = 1/2$ and $k_1 = 10^6$ s^{-1}. The downward pointing arrow in the figure indicates the inverse of a typical time resolution (100 ns) for flash-photolysis studies.[7,9,10] It is seen that the log space

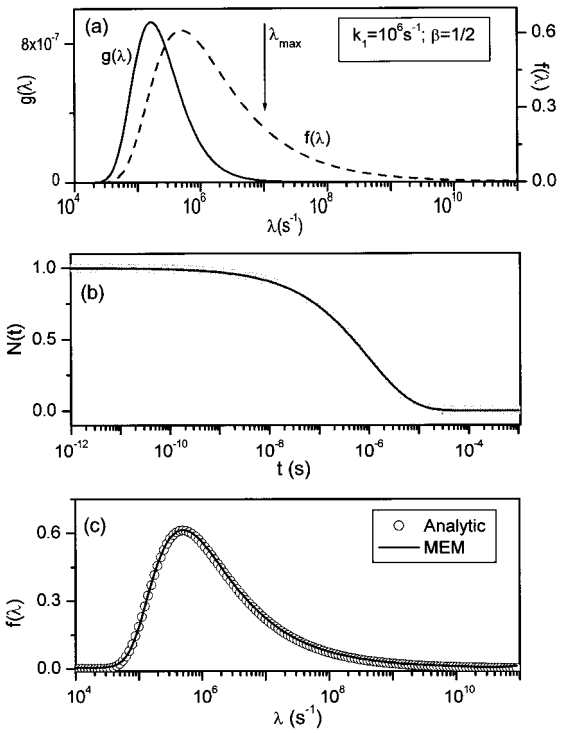

Figure 2. (a) The analytic Laplace inverse for a stretched exponential with $k_1 = 10^6$ s^{-1} and $\beta = {}^1/_2$ in linear rate space (solid line) and log rate space (dashed line). The downward pointing arrow corresponds to the inverse of a typical time resolution for flash photolysis studies. (b) Simulated stretched exponential data truncated at 10^{-12} s, along with the MEM fit (solid line). (c) The corresponding MEM rate distribution compared with the analytic distribution for the stretched exponential in log space (circles).

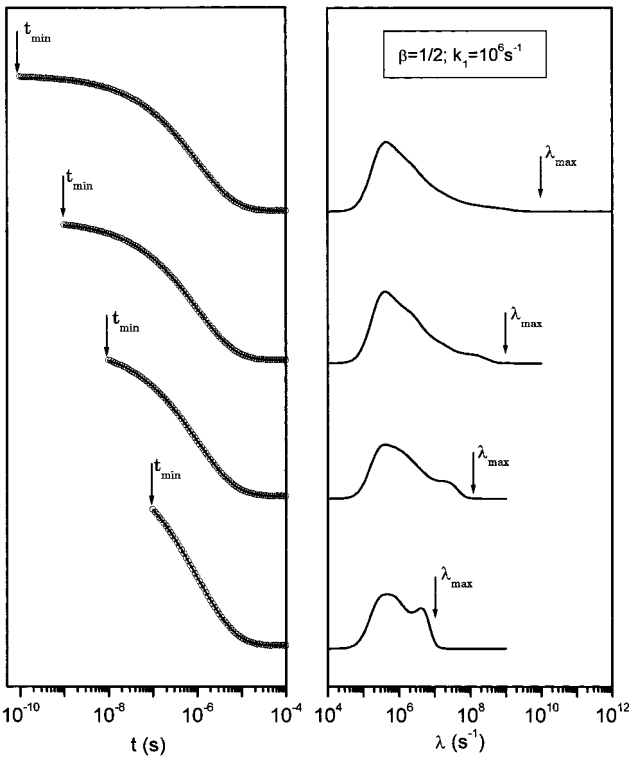

Figure 3. Left panel shows a series of simulated stretched exponential data sets, truncated from 10^{-12} to 10^{-7} s. The corresponding MEM rate distributions are shown at the right. In the region beyond λ_{max}, no experimental information is available.

distribution is nonvanishing for rates faster than 10^7 s^{-1} (inverse of the time resolution), whereas the linear distribution has negligible amplitude in this region. The presence of nonzero log space rate amplitudes in the region of the largest experimentally obtainable rates can potentially affect the MEM analysis, as we show in the following discussion. In the middle panel of Figure 2, we show the simulated stretched exponential data truncated at 10^{-12} s, along with the MEM fit. The corresponding MEM distribution is shown in the lower panel of the figure (solid line) and compared with the analytic expression in log space (circles). The agreement is seen to be almost perfect, demonstrating the efficiency of the algorithm in doing the Laplace inversion. In this case, the information needed to recover the entire rate distribution is contained within the given data set.

Next, we consider the series of MEM fits and reconstructions shown in Figure 3, corresponding to successive truncations of the data at times from 10^{-10} to 10^{-7} s, which spans some possible resolution times for flash photolysis studies. It is seen that for the MEM reconstruction of the truncated data (right panel of Figure 3), new features appear in the distribution that are quite distinct from the actual featureless distribution. The data that begins at 100 ns are seen to be most affected, with at least two distinct features that one might naively identify with separate conformational subpopulations, having mean rates given by the maxima of the peaks.

It is obvious that, for a given shortest time point t_{min} in the experimental data, we cannot expect to obtain information for rates faster than $\lambda_{max} \approx 1/t_{min}$. Thus, any features in the distribution beyond λ_{max} must be artificial. However, the surprising result of the MEM reconstructions in Figure 3 is that even the portions of the rate distribution well below λ_{max}(shown by the downward pointing arrows in the figure) are seriously distorted. Since the iterations were always stopped when χ^2 approached the optimal value of unity (for Gaussian distributed white noise), it is clear that these features are not due to overfitting the data but must arise from the truncation of the data at shorter times.

B. Simulations with a Gaussian Rate Distribution. It should be emphasized that the artifactual features in the MEM distribution appear whenever the true rate distribution has nonvanishing amplitude at λ_{max}. Thus, we must anticipate problems in the MEM reconstruction for any broad rate process with incomplete short time information. In Figure 4, we show simulations with a Gaussian rate process to illustrate this fact. A broad rate distribution with a Gaussian profile (Figure 4b, circles) was used to generate the kinetics, and the resulting temporal data was first truncated at 10^{-10} s (Figure 4a). The MEM reconstruction for these data is shown compared with the true distribution in Figure 4b (solid line) and is seen to match the true distribution very well. Now consider the data set truncated at 10^{-7} s, shown in Figure 4c, and the corresponding MEM rate distribution in Figure 4d (solid line). The presence of artifactual structure in the distribution is clearly seen. Note that the distribution below λ_{max} (10^7 s^{-1}) is again seen to be seriously distorted. The fact that false features appear in the Gaussian distributed process as well as the stretched exponential, when the data are truncated at short times, demonstrates the generality of the problems that can arise when processes with broad rate distributions are analyzed using MEM, with insufficient short time data.

The appearance of these artifacts can be traced to the fact that when a small prior level is chosen, the MEM rate distribution approaches zero for rates larger than λ_{max}. The fact that the rate distribution should approach zero beyond this value follows from the fact that the amplitudes for these rates are severely underweighted in χ^2 (see eq 2), and the optimization

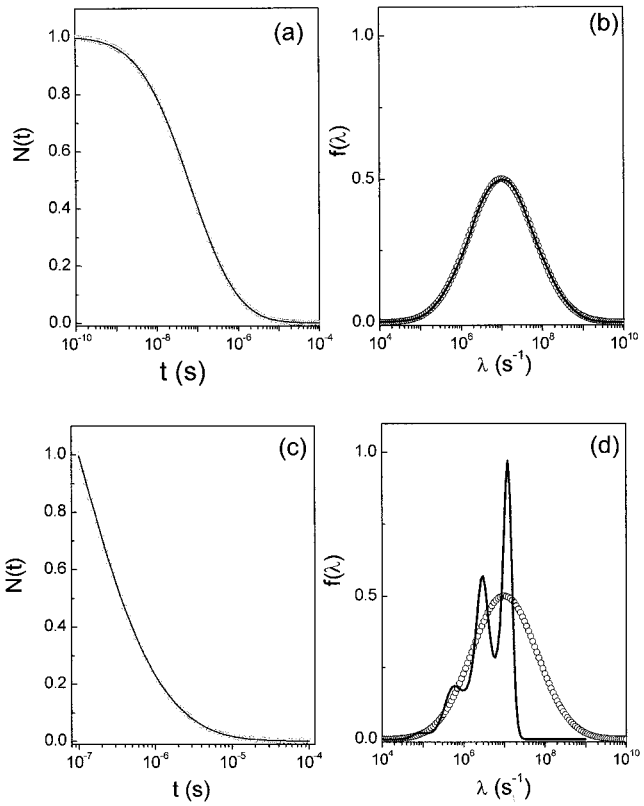

Figure 4. (a) Simulated kinetics generated using a Gaussian distribution of rates, along with the MEM fit (solid line). (b) The Gaussian distribution of rates used to generate the kinetics (circles), along with the MEM reconstructed distribution (solid line). (c) Same data as those in panel a but truncated at 10^{-7} s and renormalized to unity, as is often done experimentally. (d) Corresponding MEM reconstruction (full line) compared with the true distribution. Both the true and reconstructed distributions must be rescaled by the same factor (2.5) that was used to normalize the data in panel c. Note that the area under the MEM distribution in panel d is smaller than that for the true distribution. This arises from the fact that the MEM fit at times shorter than 10^{-7} s is imperfect and corresponds to a smaller zero time point (1.68) than the correct one (2.5) (note from eq 2 that the zero time point determines the area of the distribution). The prior distribution was set to a constant value of 10^{-4} in this simulation. If larger values for the prior distribution are used, the effective area also becomes larger and the artifacts are reduced (see text).

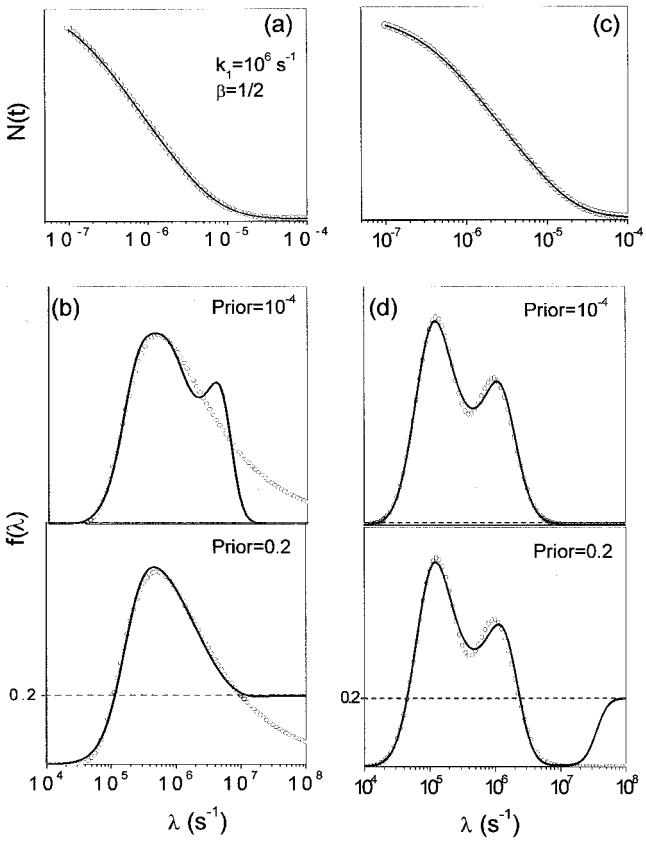

Figure 5. Role of the Prior distribution. (a) Simulated stretched exponential with $k_1 = 10^6$ s^{-1} and $\beta = 1/2$, shown truncated at 10^{-7}s. (b) Top panel shows the MEM reconstruction with a flat prior distribution of value 10^{-4}. The true distribution (from eqs 8 and 9 in the text) is shown in circles. The bottom panel shows the MEM reconstruction with larger level (0.2) for the prior distribution. (c) Kinetics simulated using a double-peaked Gaussian distribution of rates. (d) The distribution used to generate the kinetics is shown in circles. The MEM reconstruction for a small value of the prior level is shown in the top panel and for a larger value in the bottom panel (dashed line).

procedure gives back the prior distribution in the regions where no experimental information exists. In other words, the lack of required information for faster rates forces the entropy term to dominate χ^2 in the optimization. In the examples given above, the prior distribution was set to a constant value near zero ($\sim 10^{-4}$). The rate distribution approaches this small value for rates above λ_{max} and is effectively nonvanishing only before this rate. The MEM algorithm is thus forced to fit the incomplete data whose true distribution extends beyond λ_{max}, with a narrower band of rates less than λ_{max}. This is the likely cause of the discrete features that appear in the MEM reconstructions of truncated data sets.

C. Role of the Prior Distribution. As mentioned above, the MEM reproduces the prior distribution for rates faster than λ_{max}. This motivates us to consider the role of the prior distribution in the analysis. It might be expected that the use of a higher level for the prior distribution could reduce the artifactual features, since the rate distribution above λ_{max} would then not be forced to zero. In Figure 5, we show the MEM analysis using two sets of simulated data. Panel a in the figure shows the stretched exponential truncated as before at 100 ns. The corresponding MEM rate distribution is shown in panel b, using both a small (10^{-4}) and a larger (0.2) constant value for the prior distribution. The theoretical distribution is shown in circles for comparison. It is evident that use of a larger value for the prior distribution minimizes the artifactual features that appear in the MEM reconstruction. The agreement between the MEM distribution and the true distribution is quite good in this case, at least for rates below the "no-information zone" (region below $\lambda_{max} = 10^7$ s^{-1}). Above this region, the prior distribution, which was chosen to be a constant[29] (shown by a dashed line), is seen to be reproduced.

In the other simulation, a double peaked distribution of rates was used to generate the kinetics shown in panel c of Figure 5. The MEM analysis on this data set for the two different prior levels is shown in panel d,and it is seen that the MEM rate distribution is unaffected by the value chosen for the prior level. In this case, the true distribution (in log space) is within the fastest rate constant obtainable with the given data ($\lambda_{max} = 10^7$ s^{-1}) so that the features are unaffected by the chosen value of the prior level. Thus, one way of checking for the presence of false features in the MEM analysis is to obtain reconstructions for various prior distribution levels. If the features below λ_{max} in the computed rate distribution are sensitive to the prior level, then it can be concluded that they are most likely artifactual.

D. Role of the Zero Time Point. Another way to minimize the artifactual role played by rates faster than λ_{max} is to include

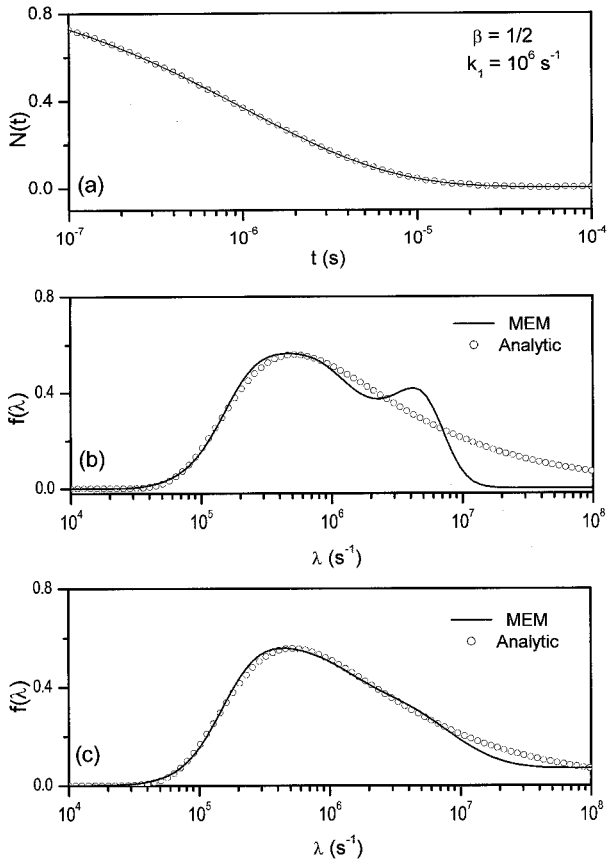

Figure 6. Role of the zero time point in minimizing the artifacts. (a) Stretched exponential kinetics truncated at 100 ns. A time zero data point has been included (not shown in the log plot) in the data set. (b) MEM reconstruction without the zero time point. (c) Shows the reconstruction with the zero time point included.

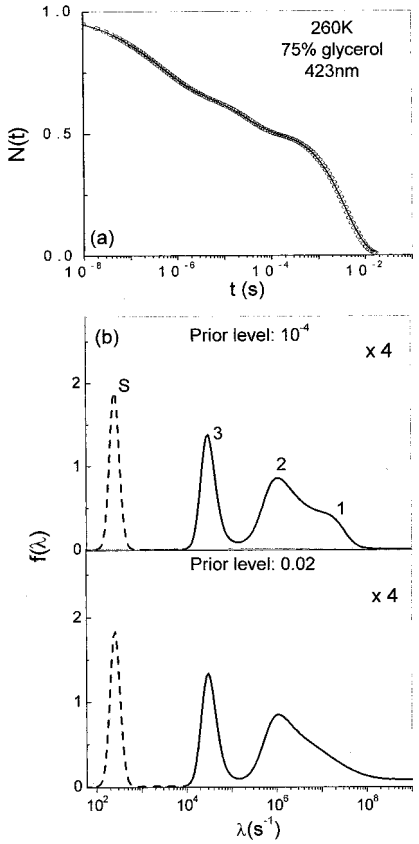

Figure 7. (a) Kinetics of CO rebinding to Mb in 75% glycerol solution, monitored in the Soret band, at 260 *K*. The MEM fit is shown in solid lines. (b) MEM rate distributions for the 260 *K* data with prior level 10^{-4} (top panel) and 0.02 (bottom panel). The bimolecular rate near 200 s^{-1} is shown rescaled in dashed lines.

an estimated zero time point in the data. This is only possible in the experimental analysis if absorption cross sections for the reactant and photoproduct states are known or can be approximated by their equilibrium values. This procedure gives an additional term in χ^2 that involves all the rate amplitudes (even those above λ_{max}), and hence, the fast rate amplitudes will not be so drastically underweighted in the fit. In Figure 6, we show the MEM fit and reconstruction for a simulated stretched exponential process, with and without the inclusion of a zero time point. It is seen in the lower portion of Figure 6 that the resulting rate distribution is flat and nonzero for rates above λ_{max} and that the artifacts are partially suppressed. With the logarithmic time base that is often adopted in flash-photolysis studies,[6,7,9,14,17] a zero time point is not usually included in the fitting procedure. However, it is sometimes possible to approximate the zero time point, by using known optical properties of the initial and photoproduct states, along with the amount of photolysis (e.g., complete photolysis[14,17]). Thus, if MEM is to be used in the kinetic analysis and short time data truncation is a possibility, it is worthwhile to include an approximate zero time point in the analysis.

E. MEM Analysis of MbCO Kinetic Data. We now consider the application of MEM to temperature-dependent studies of MbCO relaxation dynamics in solution. The binding of CO to myoglobin has been studied over a wide range of time scales and temperatures.[6,14−19] At low temperatures (T < 180 K), the protein ensemble is characterized by a "frozen" distribution of conformational substates that do not interconvert, and the rebinding process is nonexponential. An interpretation of the kinetics in this type of inhomogeneous ensemble is facilitated by a representation in rate space using MEM.[6,7] Nonexponential kinetics in myoglobin have also been observed at high temperature, where the interconversion between the substates is expected to be more rapid, and hence, the ensemble is more homogeneous on the ligand binding time scales. Thus, the nonexponential nature of the kinetics at room temperature has been attributed either to the relaxation of the proximal[15] or the distal[14] pockets, both of which lead to a time-dependent rebinding rate.

Here, we present a MEM analysis of MbCO kinetics at high temperature (260−300 K). This nonexponential geminate rebinding was previously modeled using a stretched exponential and was attributed to nonequilibrium relaxation of the distal pocket.[14] We first demonstrate the appearance of an artifactual shoulder in the portion of the MEM distribution corresponding to the fast geminate kinetics. In Figure 7, we show the kinetics of CO rebinding to myoglobin at 260 K in 75% glycerol solution, monitored at 423 nm (corresponding to the absorption maximum of the CO bound system). Shown directly below the kinetic trace is the corresponding MEM reconstruction with two different levels of the prior distribution. When the prior distribution is chosen to be constant with a small (10^{-4}) value, distinct features labeled 1−3 and S can be seen in the MEM distribution. The sharp feature in the distribution (labeled S in the figure) peaked near 200 s^{-1} is nearly exponential, and is attributed to bimolecular rebinding of CO that has escaped into solution. Peak 3 at 3×10^{-4} s^{-1} and the broader distribution consisting of the features 1 and 2 are attributed to geminate phases of the rebinding kinetics and correspond to rebinding processes taking place from within the heme pocket. Peak S at 200 s^{-1} has the largest amplitude and has been shown rescaled

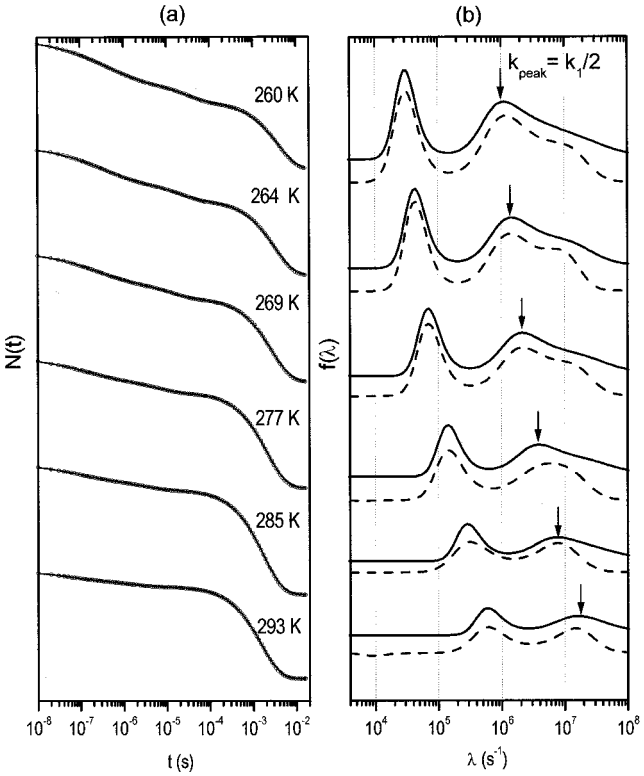

Figure 8. (a) Soret band MbCO kinetics for the temperatures in the range 260−293 K (circles), shown along with the MEM fits (solid lines). (b) Corresponding MEM rate distributions. Only the geminate processes are shown. The corrected distributions (using larger value 0.02 for the prior level) are shown in solid lines. The artifactual distributions are shown as dashed lines (prior = 10^{-4}). The arrows indicate the peaks used to extract the stretched rate constants associated with the asymmetric distribution, as described in the main text.

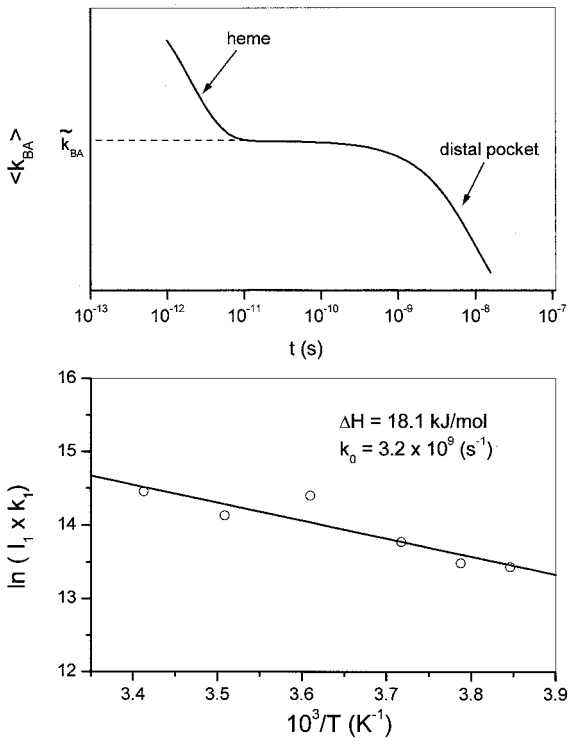

Figure 9. (a) Schematic of the behavior of the fluctuationally averaged (time dependent) rate constant for ligand rebinding to the heme $\langle k_{BA} \rangle$ depicted over the time scales of heme and distal pocket relaxations. (b) Temperature dependence of $\tilde{k}_{BA} \approx I_1 k_1$. I_1 was found from the area under the asymmetric distributions in Figure 8. The solid line shows a linear fit to the plot. The slope gives the enthalpy barrier height associated with $\tilde{k}_{BA}$, and the intercept is related to the prefactor.

for clarity. The shoulder labeled 1 is quite distinct and could potentially be attributed to a conformational subpopulation. However, when the prior level is increased to a higher value of 0.02, it is seen that the shoulder disappears, showing that it is an artifact resulting from incomplete short time data. We conclude that the shoulder is due to the existence of nonzero amplitudes of the true rate distribution near the fastest obtainable rate of 10^8 s^{-1}. This example illustrates the need for caution in the interpretation of the MEM reconstruction when data are truncated at times where the rate amplitudes may be nonzero.

It is clear from the corrected distributions (using the larger prior values) shown in Figure 7 that the geminate rebinding kinetics is governed by an asymmetric distribution of rate amplitudes and that there are rate components faster than $\lambda_{max} = 10^8$ s^{-1}. We note that in a previous application of MEM to analyze the low-temperature MbCO rebinding kinetics,[10] three distinct features were observed in the rate distribution for the data taken at 250 K, the highest temperature kinetics measured in that study. In contrast to the asymmetric distribution seen here for the fast phase of the geminate kinetics, Johnson et al.[10] observed a single Gaussian-like distribution of rates. This difference can possibly be attributed to the better experimental time resolution of the data presented here (10^{-8} s, compared to 10^{-7} s). It is also conceivable that the difference in temperatures (250 vs 260 K) at which the kinetics were monitored might contribute to this discrepancy.

In Figure 8, we display the MEM analysis of the MbCO rebinding kinetics over the temperature range of 260−293 K. Only the geminate part of the rate distribution is shown, analyzed using two prior levels (solid line, using larger prior levels, and dashed line, using small prior levels). We note from this figure that for higher temperatures, the artifactual features that appear when small prior values are used become less prominent, indicating that the rate distribution gets narrower and more symmetric at higher temperatures. In view of a previous study, where the geminate rebinding was modeled using a stretched exponential,[14] along with the results of eqs 8 and 9 and Figure 2, we suggest that the asymmetric MEM distributions between 260 and 280 K in Figures 7 and 8 are indicative of a geniune stretched exponential behavior for the MbCO geminate kinetics.

Under the assumption that the short time nonexponential behavior arises due to a series type of relaxation (time-dependent rates), we can recover the enthalpy barrier for CO rebinding to the heme using the MEM distribution and compare it with previous results.[14] For this purpose, we note that the rate constant that is most easily linked to the low-temperature rate distribution[16] is associated with CO geminate rebinding to the relaxed heme, prior to distal pocket (or protein) relaxation.[14] Figure 9a schematically depicts the behavior of the average rate constant for rebinding, as discussed by Tian et al.[14] Here it is assumed that the heme relaxation is a picosecond process, while the distal pocket (or protein) relaxation takes place on nanosecond time scales. The (approximately) constant rebinding rate labeled $\tilde{k}_{BA}$ in the figure can be predicted[30,31] from the rate distributions obtained at low temperature,[16] where the heme partially relaxes to an intermediate out of plane position[32,33] and distal pocket (or protein) relaxation is completely quenched. The fundamental rate constant $\tilde{k}_{BA}$ can be related to the observed stretched rate constant k_1 using $\tilde{k}_{BA} = I_1 k_1$, where $I_1$is the (normalized) amplitude of the stretched exponential decay. Assuming that $\beta = {}^1/_2$, the stretched rate constant k_1 can be obtained from the

MEM distribution using the fact that the log rate space distribution for a stretched exponential is peaked at $k_{peak} = k_1/2$ (as follows from eqs 11 and 12). The peaks of the distributions that were used to obtain k_1 are indicated by downward pointing arrows Figure 8. The amplitudes I_1 are calculated from the areas under the asymmetric peaks. The values of $\tilde{k}_{BA} = I_1 k_1$ extracted from the MEM analysis are shown using an Arrhenius plot in Figure 9b. The slope of this plot is found to be $E_A \approx 18$ *kJ*/mol and gives the barrier height for CO rebinding near room temperature after heme relaxation is complete, but prior to distal pocket (or protein) relaxation. The high-temperature intercept gives a prefactor $k_0 \approx 3 \times 10^9$ s^{-1}. These results are in good agreement with the predictions of a simple model[30,31,14] and with previously obtained values,[14] suggesting that the identification of the asymmetric MEM distribution with a stretched exponential process is valid.

F. MEM Analysis of Ultrafast Photophysical Processes (Mb and MbNO). In this section, we consider the application of MEM to the analysis of the ultrafast photophysics of myoglobin, monitored through pump−probe femtosecond coherence spectroscopy[34,35] (FCS). Traditional nonlinear least-squares fitting procedures of kinetic data often suffer from problems due to local minima and overfitting (in addition to being model specific) and can lead to inconsistent results. Furthermore, FCS data often contain oscillatory signals superimposed on the exponential background decay signal. These oscillations are a manifestation of the quantum beats induced in the medium by the pump pulse interaction.[35] The extraction of the rate constants for the "zero frequency" background decays from the total FCS data often poses a challenge due to the presence of the oscillatory signals that act as a systematic noise. We have found that the bipolar MEM algorithm, with the pulse convolution feature (see Methods section above), offers a consistent approach in separating the nonoscillatory background from the oscillatory components of the pump−probe signal.

The results of the MEM analysis of the open band FCS signals of MbNO are shown in Figure 10. (Open band measurements are obtained by registering the entire probe pulse bandwidth on the photodetector, without the use of a monochomator to filter its spectral content, as is sometimes done to enhance higher-frequency oscillatory components of the FCS signal.[34,35]) A series of open band pump−probe data for carrier wavelengths in the range 400−500 nm (resonant with the Soret band) are shown along with the MEM rate distributions. The kinetics shown are presented in arbitrary units of the net transmission change (pump-on minus pump-off) of the probe pulse. Positive signals correspond increased transmittance (or decreased absorbance) following pump photoexcitation (bleaching). Negative signals correspond to a decreased transmittance of the pump induced photoproduct (anti-bleach). The data at 413 and 420 nm have been offset by a small constant in order to remove the large background in the MEM rate distribution at longer time constants, which corresponds to NO recombination following photolysis. The data near zero delay and extending beyond the width of the pulse autocorrelation (∼150 fs) have been excluded from the present analysis. This region corresponds to the overlap of the pump and probe pulses and contains a strong nonlinear response known as the coherent coupling signal, which will not be considered here.[36] The corresponding rate distributions for each independently analyzed data set stretch over three decades (0.01 to 10 ps) and are plotted as distributions in the time constant (inverse rates) in the right panel of Figure 10. Positive peaks correspond either to decay of a bleached signal or the rise of an anti-bleaching signal.

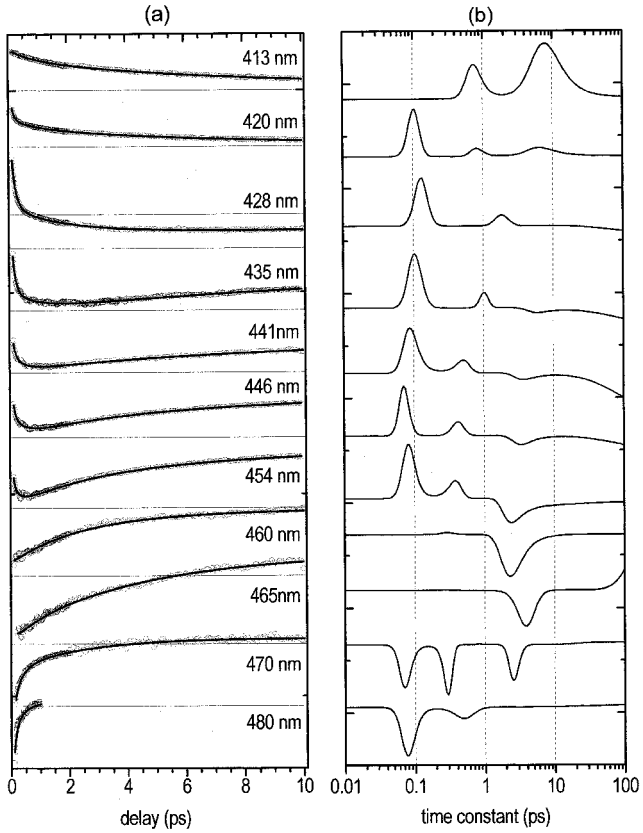

Figure 10. (a) Series of MbNO open band data (circles) for different probe wavelengths, along with the corresponding MEM fits (solid line). The broad offsets occurring near 100 ps have been subtracted for efficient recovery of picosecond rates. (b) The corresponding MEM rate distributions.

Negative peaks correspond to bleaching buildup or the decay of antibleach signal. The change from a positive to a negative amplitude for a given peak as a function of the probing wavelength occurs at an isosbestic point between the equilibrium and nonequilibrium absorption spectra. It is noteworthy that the rate distributions for all the kinetics are relatively narrow (see Figure 1 and related discussion above), suggesting that exponential processes are sufficient to describe the observed signals.

From the MEM analysis presented in Figure 10, it is clear that the kinetics can be classified into three major groups, with time constants 0.1, 0.5−1, and 2−4 ps. A resolution of the peak corresponding to rate processes larger than 10 ps (such as NO recombination) requires longer delay scans than presented here. It is seen that all the kinetics in the wavelength range of 400−427 nm exhibit a bleaching signal. Between 427 and 430 nm, we observe a transition from the bleach into antibleach phase, and the signal remains in the antibleaching region until full recovery. In the range 435−454 nm, only the antibleaching signals are recorded, while the kinetics measured at 460, 470, and 480 nm show an antibleach that evolves into a bleaching signal. It must be mentioned that the equilibrium difference spectrum (Mb-MbNO) has a second isosbestic point near 455 nm and shows a bleach for longer wavelengths.

In Figure 11, we present the open band measurements of deoxy Mb (Mb) along with the corresponding MEM analysis. It is noteworthy that the kinetics have features very similar to that of MbNO despite the absence of photolysis in Mb, which is a five-coordinate species. In the case of Mb, the kinetics is composed of two major components, with time constants in the ranges 0.1−0.3 and 2−6 ps. The major difference between the kinetics of the two compounds is the absence of a slower process

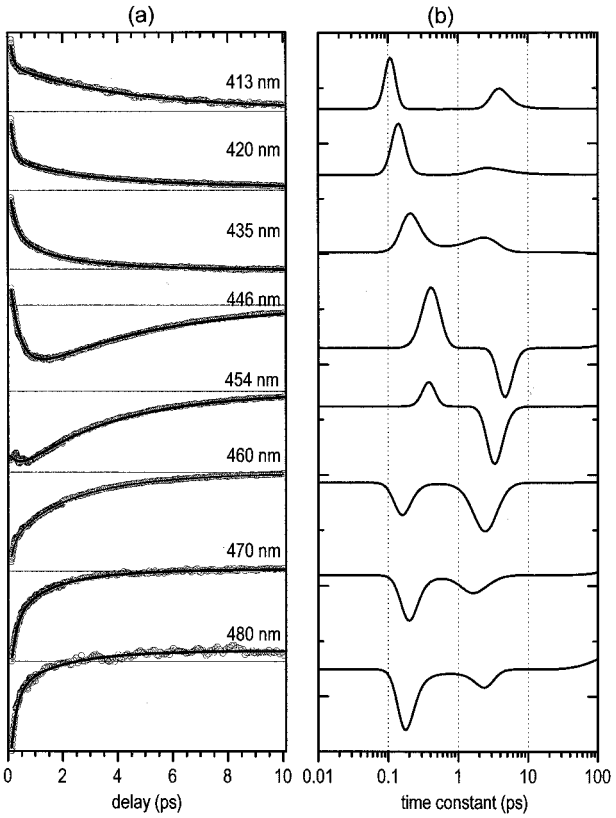

Figure 11. (a) Series of deoxyMb open band data (circles) for different probe wavelengths, along with the corresponding MEM fits (solid line). The broad offsets occurring near 100 ps have been subtracted for efficient recovery of picosecond rates. (b) The corresponding MEM rate distributions.

that corresponds to ligand recombination in MbNO (not shown, to be published).

In interpreting the open band data of Mb and MbNO, it must be kept in mind that the absorption spectrum of the pump induced photoproduct is dynamic rather than static in nature, as revealed by ultrafast transient spectral measurements using a white light continuum.[42] As might be expected, it is found that the dynamics of the first and second moments of the spectral line shape of the pump induced photoproduct have time constants similar to those found in the single wavelength open band measurements discussed above. In general, there are three major dynamical processes that are observed in the transient line shape evolution. These consist of the ligand recombination with time constant 10−100 ps, spectral shifting of the transient photoproduct Mb* (change in the peak position of the line shape) with time constant 2−6 ps, and spectral narrowing of Mb*(change in the width of the line shape) with a time constant of 0.1−0.3 ps. The observed open band kinetics for each wavelength shown in Figures 10 and 11 is a result of a combination of these processes. The observed kinetics is highly dependent upon the location of the probe wavelength with respect to the equilibrium and photoproduct absorption spectra (which is dynamic). For instance, note the disappearance of the fast bleaching decay and anti-bleaching rise seen in the MbNO kinetics at 413 and 460 nm. These two wavelengths correspond to the points where the photoproduct absorption remains unchanged despite the dynamic spectral evolution. Such phenomena are "dynamic isosbestic points" that result from a combination of spectral narrowing and shifting of the photoproduct absorption spectrum. There are two competing models that can account for the observed spectral dynamics. One is based on the creation of a "hot" electronic ground state of the photoproduct and its subsequent cooling.[38−41,43] The second model is based on the creation of multiple electronically excited intermediate state species that have red shifted spectra, followed by decay to the final photoproduct ground state.[37] A careful analysis of the femtosecond continuum spectra[42] favors the hot ground-state model over the multistate model, as does the recent time resolved Raman data of Kitagawa and Mizutani.[44]

IV. Summary

In the analysis of nonexponential kinetic processes, the MEM is well established as a useful tool for obtaining rate distributions with minimal noise induced features. However, as the simulations presented in this paper show, truncation of short time data points can introduce distinct features even in the optimal ($\chi^2 = 1$) reconstruction. These features extend into the slower regions of rate space and can potentially affect the interpretation of the MEM distribution. In this paper, we have demonstrated how, in the absence of short time information, the prior distribution in the entropy functional can be used to distinguish true features from false ones. An experimentally approximated zero time data point can also be useful in minimizing the appearance of misleading features in the MEM rate distribution. We also stress that when noise is present, even pure exponential processes have broad MEM distributions so that further tests are required to check for nonexponential behavior. An application of MEM to the nanosecond geminate kinetics of MbCO rebinding near room temperature yields an asymmetric rate distribution that is characteristic of stretched exponential behavior. The value obtained for the barrier height (prior to distal pocket structural relaxation), $E_A \sim 18$ kJ/mol, agrees well with previously obtained results.[14]

Finally, we have also demonstrated the application of a bipolar MEM algorithm (with a pulse convolution feature) that can extract positive and negative rate amplitudes from femtosecond pump−probe data. The MEM analysis of single wavelength pump−probe data on myoglobin has revealed the existence of at least three distinct rate processes, which are consistent with independent studies that employ continuum probe techniques.[42] Surprisingly, the ultrafast photophysics of Mb and MbNO appear to be governed by exponential rather than distributed processes, as indicated by the relatively narrow rate distributions found in the ultrafast kinetics. An independent analysis of the continuum probe data[42] favors a "hot" dynamic line shape model associated with the cooling of the transient photoproduct. A more detailed analysis of these results will be reported elsewhere.

Acknowledgment. This work is supported by grants from NSF (MCB 9904515) and NIH (DK35090).

References and Notes

(1) McWhirter, J. G.; Pike, E. R. *J. Phys A: Math. Gen.* **1978**, *11*, 1729.

(2) Tichonov, A.; Arsenin, V. *Solutions of Ill-posed Inverse Problems;* John Wiley & Sons: London, 1977.

(3) Jaynes, E. T. In *Papers on Probability, Statistics and Statistical Physics*; Rosenkranz, R., Ed., Ed.; D. Reidel: Dordrecht, The Netherlands, 1983.

(4) Livesey A. K.; Brochon. J. C. *Biophys. J.* **1987**, *52*, 693.

(5) Sibisi, S. *Nature (London)* **1983**, *301*, 134.

(6) Steinbach, P. J.; Ansari, A.; Berendzen, J.; Braunstein, D.; Chu K.; Cowen, B.; Ehrenstein, D.; Frauenfelder, H.; Johnson, J. B.; Lamb, D. C.; Luck, S.; Mourant, J. R.; Nienhaus, G. U.; Ormos, P.; Phillip, R.; Xie, A.; Young, R. D. *Biochemistry* **1991**, *30*, 3988.

(7) Steinbach, P. J.; Chu, K.; Frauenfelder, H.; Johnson, J. B.; Lamb, D. C.; Nienhaus, G. U.; Sauke, T. B.; Young, R. D. *Biophys. J.* **1992**, *61*, 23.

(8) Petrich, J. W.; Lambry, J. C.; Balasubramanian, S.; Lambright, D. G.; Boxer, S. G.; Martin, J. L. *J. Mol. Biol.* **1994**, *238*, 437.
(9) Tetreau, C.; Primo, C. D.; Lange, R.; Tourbez, H.; Lavalette, D. *Biochemistry* **1997**, *36*, 10262.
(10) Johnson, J. B.; Lamb, D. C.; Frauenfelder, H.; Mueller, J. D.; McMohan, B.; Nienhaus, G. U.; Young, R. D. *Biophys. J.* **1996**, *71*, 1563.
(11) Livesey, A. K.; Skilling, J. *Acta Crystallogr., Sect. B: Struct. Crystallogr. Cryst. Chem.* **198**, *A1*, 113.
(12) Ngai, K. L.; Wang, C. H.; Fytas, G.; Plazak, D. L.; Plazak, D. J. *J. Chem. Phys.* **1987**, *86*, 4768.
(13) Frauenfelder, H.; Sligar, S. G.; Wolynes. P. G. *Science* **1991**, *254*, 1598.
(14) Tian, W. D.; Sage, J. T.; Srajer, V.; Champion, P. M. *Phys. Rev. Lett.* **1992**, *68*, 408.
(15) Ansari, A.; Jones, C. M.; Henry, E. R.; Hofrichter, J.; Eaton, W. A. *Science* **1991**, *256*, 1796.
(16) Austin, R. H.; Beeson, K. W.; Eisenstein, L.; Frauenfelder, H.; Gunsalus, I. C. *Biochemistry* **1975**, *14*, 535.
(17) Tian, W. D.; Sage, J. T.; Champion, P. M.; Chien, C.; Sligar, S. G. *Biochemistry* **1996**, *35*, 3487.
(18) Post, F.; Doster, W.; Karvounis, G.; Settles, M. *Biophys. J.* **1993**, *64*, 1833.
(19) Lambright, D. G.; Balasubramanian, S.; Boxer, S. G. *Chem. Phys.* **1991**, *158*, 249.
(20) Skilling, J.; Bryan R. K. *Mon. Not. R. Astron. Soc.* **1984**, *211*, 111.
(21) Stephenson, D. S. *Prog. NMR Spectrosc.* **1988**, *20*, 51.
(22) Press. W. H.; Teukolsky, S. A.; Vetterling, W. T.; Flannery. B. P. *Numerical Recipes in C*, 2nd ed.; Cambridge University Press: Cambridge, 1992.
(23) Laue, E. D.; Mayger, M. R.; Skilling, J.; Staunton, J. *J. Magn. Reson.* **1986**, *68*, 14.
(24) Smith, P. F.; Player, M. A. *J. Phys. D: Appl. Phys.* **1991**, *24*, 1714.
(25) For instance, the Hessian now takes the form $(\nabla\nabla Q)_{ij} = G(\lambda_i,t) \times G(\lambda_j,t)$.
(26) The number of data points decreased with increasing truncations. But the MEM is quite insensitive to the number of data points. and we can ignore this factor in the present discussion.
(27) Stephenson, M.; Radmore, P. M. *Advanced Mathematical Methods for Engineering and Science Students*; Cambridge University Press: Cambridge, 1990.
(28) Lindsey, C. P.; Patterson, G. D. *J. Chem. Phys.* **1980**, *73*, 3348.
(29) Although we have considered a constant prior distribution in this analysis, the discussion here is not restricted to this choice in that a prior distribution of any shape will be reproduced in the region where no experimental information is available.
(30) Srajer, V.; Reinisch, L.; Champion. P. M. *J. Am. Chem. Soc.* **1988**, *100*, 6656.
(31) Srajer, V. Ph.D. Thesis, Northeastern University, 1991. Srajer, V.; Champion, P. M. *Biochemistry* **1991**, *30*, 7390. Champion, P. M. *J. Raman Spectrosc.* **1992**, *23*, 557.
(32) Schlichting, I.; Berendzen, J.; Phillips, G. N., Jr.; Sweet, R. M. *Nature* **1994**, *371*, 808.
(33) Teng, T. Y.; Srajer, V.; Moffat, K. *Nat. Struct. Biol.* **1994**, *1*, 701.
(34) Rosca, F.; Kumar, A. T. N.; Ye, X.; Sjodin, T.; Demidov, A. A.; Champion, P. M. *J. Phys. Chem.* **2000**, *104*, 4280.
(35) Kumar, A. T. N.; Rosca, F.; Widom, A.; Champion, P. M. *J. Chem. Phys.* **2001**, *114*, 701.
(36) The presence of the coherent coupling signal near the zero delay region might affect the ultrafast medium response over and above the simple pulse convolution considered here. Although we have chosen to ignore this portion of the data in the present analysis, a more complete understanding of the nonlinear response near zero delay is necessary in order to accurately and reliably extract the fast electronic decay processes occurring on the time scales of the pulse durations and will be considered in future work.
(37) Petrich, J. W.; Poyart, C.; Martin, J. L. *Biochemistry* **1988**, *27*, 4049. Franzen, S.; Kiger, L.; Poyart, C.; Martin, J.-L. *Biophys. J.* **2001**, *80*, 2372.
(38) Rodriguez, J.; Kirmaier, C.; Holten, D. *J. Chem. Phys.* **1991**, *94*, 6020.
(39) Rodriguez, J.; Holten, D. *J. Chem. Phys.* **1990**, *92*, 5944.
(40) Rodriguez, J.; Holten, D. *J. Chem. Phys.* **1989**, *91*, 352.
(41) Rodriguez, J.; Westerfield, W.; Whiteley, B.; Kirmaier, C.; Holten, D. *J. Lumin.* **1994**, *60−1*, 507−510.
(42) Demidov, A. A.; Ye, X.; Rosca, F.; Kumar, A. T. N.; Champion, P. M. in press.
(43) Wang, W.; Ye, X.; Demidov, A. A.; Rosca, F.; Sjodin, T.; Cao, W.; Sheeran, M.; Champion, P. M. *J. Phys. Chem. B* **2000**, *104*, 10789.
(44) Mizutani, Y.; Kitagawa, T. *Chem. Record* **2001**, *1*, 258.